ELSEVIER

Geomorphology 22 (1998) 159–180

GEOMORPHOLOGY

Slope effect on saltation over a climbing sand dune

Bruce R. White [a,*], Haim Tsoar [b]

[a] *Department of Mechanical and Aeronautical Engineering, University of California, Davis, CA 95616, USA*
[b] *Department of Geography and Environmental Development, Ben-Gurion University of the Negev, Beer-Sheva, Israel*

Received 29 November 1995; revised 15 October 1996; accepted 27 February 1997

Abstract

Results from a three-year study are presented that integrate field work (in Israel), physical modeling (wind-tunnel testing at UC Davis), and numerical solutions of grain trajectories to model and explain sand transport over a climbing dune. Field grain-size analyses of surface- and saltation-trap materials taken along various positions of the slope suggest that only smaller particles (< 230 μm in diameter for a friction speed, u_*, equal 30 cm/s) were able to climb a 20 degree slope in an escarpment normal to the prevailing strong wind direction. Numerical solutions of the particle trajectories are in good agreement with field measurements and confirm that particle motion is diminished at the base area of the slope and that the motion of larger-sized particles is completely terminated which causes an accumulation of these particles. The results suggest that the transport of the majority of the larger particles (> 230 μm) is by saltation. The model is numerically extended to a general series of slopes, particle sizes, and friction speeds with similar tends exhibited. © 1998 Elsevier Science B.V.

Keywords: sand; dunes; saltation; sediment transport; eolian features; wind transport

1. Introduction

The transport of surface material in nature generally occurs on sloped surfaces (i.e., rippled surfaces, sand dunes, and larger-scale topographical surface changes, etc.) and not on horizontal surfaces. Relatively few studies, whether laboratory-, computer- or field-based, have assessed the effect of slope on the initiation of particle motion and subsequent transport.

The formation and movement of sand dunes are, to a large extent, controlled by the effect of slope on grain transport. Sand moves up the windward side of the dune and then is deposited on the leeward area. In this process, sand must be transported both 'uphill' and 'downhill' as the sand dune moves in position. Sand dunes have a convex shape with different aspect ratios of h/L (h = the height of the dune, and L = the characteristic dune horizontal width or length). As a result of these types of processes, most sand transport occurs on slopes with inclinations between zero and the angle of repose which is about 33° for most sand-sized material (Tsoar, 1985; Pye and Tsoar, 1990; Burkinshaw et al., 1993). Topographical obstacles give rise to perturbations in the flow, which in turn generate variations in shear stress (Taylor and Gent, 1974; Jackson and Hunt, 1975; Jensen and Zeman, 1985; Hunt et al., 1988a; Hunt et al., 1988b).

* Corresponding author. E-mail: brwhite@ucdavis.edu

PII S0169-555X(97)00058-5

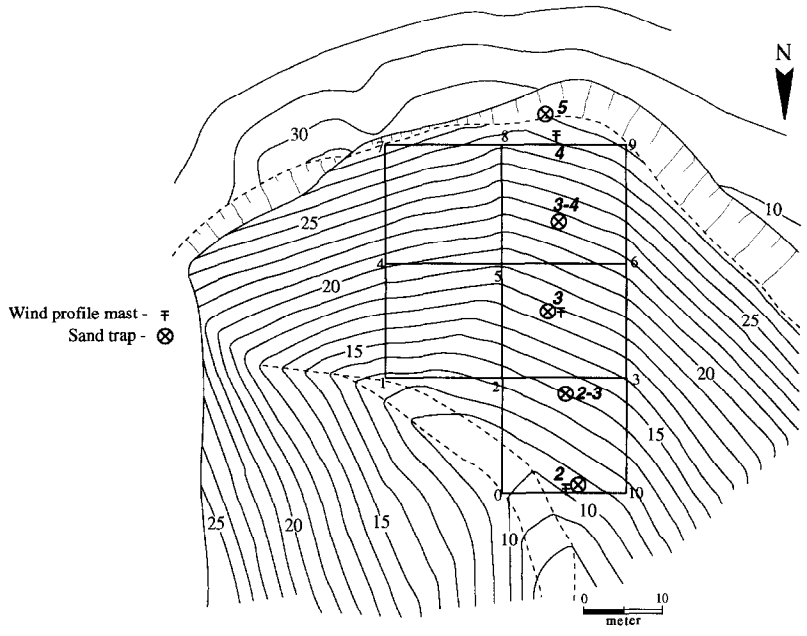

Fig. 1. Topographic map of the climbing dune in the Negev Desert. Contour elevations are given in meters. The squares on the map link reference points marked in the field. The bold numbers indicate the location where sand samples were retrieved from the surface and from sand traps and where wind profile measurements were taken.

Few theoretical models exist which combine the vector of forces exerted on grains by wind on a sloped surface with variations in shear velocity and turbulence characteristically ensuing from flow over slopes. Most work which recognized the problem (e.g., Lancaster, 1985; Walmsley and Howard, 1985; Hardisty and Whitehouse, 1988; Mulligan, 1988; Wiggs, 1993) did not give sufficient resolution to change in shear stress or implications to the resulting transport of sand over a slope.

Wipperman and Gross (1986) developed a numerical model of the shaping and migration of an isolated barchan dune. They calculated the steady-state wind field using a meso-scale simulation model from which the friction-speed distribution is determined. Sand transport, using the calculated friction speeds, was estimated by the equation of Lettau and Lettau (1978) which led to net erosion and depositional areas, thus forming the barchan dune. More recently, laboratory studies done by Iversen and Rasmussen (1994) assessed the effect of the slope on the threshold speed but did not consider changes in shear stress along the slope.

White and Tsaor have developed a theoretical model of aeolian sediment transport on slopes. This has been accomplished by numerical analysis of the equations of aeolian sand transport on slopes. Field work conducted in the Negev Desert of Israel measured changes in wind profile and sand transport over a climbing dune. Wind-tunnel measurements on a model of the climbing dune provided variation of wind flow for usage in an empirical model. The climbing dune in the field was about 20 m high and had a slope of about 20° (Fig. 1). The numerical and experimental results have the same geometric shape and slope as those in the field.

2. Field measurements: methods and results

2.1. Generation of field maps

A topographic map of a climbing dune was prepared (May 1991) through an accurate survey of the dunes with an electronic theodolite. The scale of the map was 100:1 with contours in 1-m intervals. A three-dimensional model, on which wind-tunnel wind-profile measurements were acquired, was constructed from relative elevation changes taken from

the topographic map to acquire wind profiles. The uncertainty of the wind-tunnel model was estimated at ±5% of the true dune-geometry.

Eleven reference points were located in the field and on the map, expediting placement of field measuring or sampling points (Fig. 1). Contours on the topographic map were generated from computerized data. Fig. 1 illustrates the dune shape and the location of the coordinate system. All field measurements were performed on the climbing dune at these eleven field reference points.

2.2. Sand flux

Measurements of sand flux were obtained using vertical traps similar to a trap developed by Leatherman (1978) and modified and enlarged by Rosen (1979). Sand traps were modified to accommodate field conditions. Each trap consisted of a 10 cm diameter by 100 cm long PVC tube which was partially buried. The exposed 50 cm had two slits that extended 46 cm down from the top. One slit (8 cm wide) served as a collection orifice and the back slit (10 cm wide) was covered with 60 μm screening to maximize exit flow. A tube liner, which was easily removable, served as the sand collector. A fine screen covering the base of the liner allowed rain water to drain away without effecting material collection. The Leatherman type trap is not 100 percent efficient, because of flow interference and scouring. In the present case no noticeable scouring was observed during the course of the experiments. All traps were installed in a vertical position.

Seven traps were deployed during both summer and winter months along the climbing dune. One of the deployments was in winter when the wind blew from primarily west and north directions, with speeds above the annual average. The other deployments of the traps were during summer when wind was entirely from north with magnitudes just above the threshold speed which was about 6 m/s. The deployment position of the traps is illustrated in Fig. 1. The location of the traps is given in x/L where x is the distance of the trap from the crest of the dune and L is the entire length of the dune slope. The 'crest' of the dune was at $x/L = 0$, and the base of the dune was at about $x/L = -1.0$. Traps were located at $x/L = -0.96$, -0.76, -0.55, -0.34, and -0.13.

2.3. Sand texture

Sand texture is a very sensitive factor that reflects changes in the transportation capacity of the wind. For the present work, the particle-size diameter was measured in the phi (ϕ) grade scale where $2^{-\phi} = d$, and d is the grain size in mm.

A sufficient strong wind blowing over a sandy surface will pick up sand grains and cause them to skip along the surface in a series of short flat trajectories. At each impact, those bounding grains, on average, eject grains, which in turn begin to hop across the surface. This phenomenon is known as saltation (White and Schulz, 1977; White, 1982). Saltation is characterized mostly by grains in the range of fine sand (125–250 μm or 2–3 ϕ). Suspension is characterized by grains < 74 μm or > 3.75 ϕ (dust) which are carried for large distances by the wind flow. The range between these two modes (74–125 μm or 3–3.75 ϕ) is where grains display trajectories between saltation and suspension and are known as modified saltation (Tsoar and Pye, 1987).

The desert atmosphere can be 'heavy' with many particles in suspension (dust). Active desert sand dunes, however, contain no more than 3% of particles < 74 μm or > 3.75 ϕ (Tsoar, 1976) that enter into the suspension mode through the impingement of the saltating grains. Sharp-edged dunes, such as most seif and transverse dunes, are composed of well-sorted modes of fine sand, whereas the plinth of dunes, interdune areas, and low-flat dunes such as sand sheets and zibars consist of bi-modal sand (Pye and Tsoar, 1990; Tsoar, 1986). One of the objectives of the present work was to obtain measurements of grain-size distribution along a climbing dune.

Larger particles can be moved by strong winds resulting in large values of surface stress that occur on the upper portion of the climbing dune slope. Opposing this is the additional effect that gravity has on these grains which depends on the weight component ($mg \sin \theta$), acting against the wind direction.

2.4. Grain-size analysis

Fifty samples of sand were retrieved from the field. Samples from various parts of the climbing dune were compared with those from other dunes in the area that do not 'climb' and from the sand traps

Table 1
Average grain-size and standard deviation of the sampled sand

Date	Location #	Average grain-size of surface sand (in ϕ)	Average grain-size of trapped sand (in ϕ)	Standard deviation of surface sand (in ϕ)	Standard deviation of trapped sand (in ϕ)
12 July 1993	2	2.16		0.534	
	2/3	2.50	2.88	0.542	0.520
	3	2.51	2.98	0.537	0.458
	3/4	2.59	2.94	0.406	0.371
	4	2.69	2.92	0.356	0.346
16 July 1993	2	2.33		0.562	
	2/3	2.41	2.85	0.506	0.499
	3	2.53	2.91	0.501	0.472
	3/4	2.66	2.92	0.425	0.364
	4	2.62	2.81	0.389	0.355
11 Aug. 1993	2				
	2/3	2.50	3.02	0.525	0.514
	3	2.51	2.89	0.502	0.456
	3/4	2.63	2.85	0.425	0.365
	4	2.64	2.69	0.410	0.406
6 Feb. 1994	2	2.20	N/A	0.427	N/A
	2/3	2.61		0.544	
	3	2.58		0.531	
	3/4	2.53		0.506	
	4	2.57		0.433	
12 July 1994	2	2.40		0.561	
	2/3	2.62	2.83	0.473	0.441
	3	2.64	2.85	0.421	0.439
	3/4	2.70	2.70	0.411	0.385
	4	2.74	2.77	0.407	0.357

that were deployed on the slope of the climbing dune. The grain-size distribution was obtained by means of standard sieves suspended on a shaker. The aperture of each sieve was greater by 1/4 ϕ than the one above. The results show the distribution in percentage of the grain sizes (see Table 1).

Sand was sampled on the climbing dune to determine the differences between surface dune sand and sand trapped in the saltation mode. First, sand traps were placed to collect saltating sand; second, samples were collected directly from the surface of the dune near the traps. The samples from the climbing dune sand trap indicated sand in a state of transport and erosion (saltation), whereas the samples from the surface of the dune indicated the deposition mode (surface-dune sand). Rates of transport, erosion and deposition were monitored by means of erosion pins staked along two lines, one along points # 2, 5 and 8 and the other along points # 6–9 (Fig. 1). The erosion pins along two parallel lines yielded measurements for rates of erosion and deposition.

The grain-size distribution of samples of sand retrieved from the field were bi-modal with coarse and fine modes. Sand samples from sand traps, that were deployed along the climbing dune during the winter period, showed an abrupt decrease in the coarse mode with an increase in the fine mode both as a function of increasing height upward along the surface of the dune (Fig. 2). The wind direction during this period was from the north, northeast, and west. By comparing the grain-size distribution between the surface and the trap collected on July 11–12, 1993 at point # 2/3, the surface sand has only the coarse mode and is, therefore, in a state of erosion; conversely, the trap sand with the fine mode is in a deposition state (Fig. 3).

Results of the grain-size distribution of sand trapped (saltation mode) during the summer period (Fig. 4) as compared with sand sampled on the surface of the dune near the collectors (Fig. 5) show the difference between erosion and deposition. The surface-sand samples (depositional mode) were

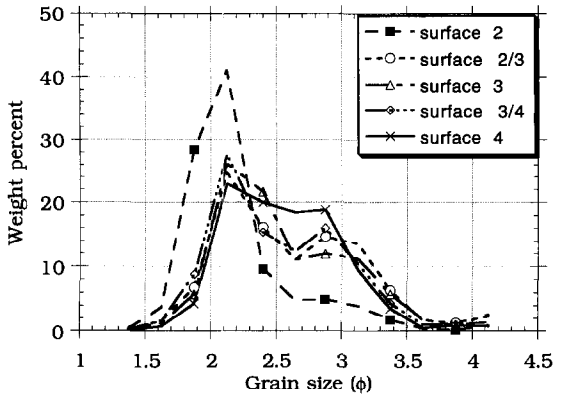

Fig. 2. Grain-size distribution of sand samples retrieved from the slope of the climbing dune in February 1994.

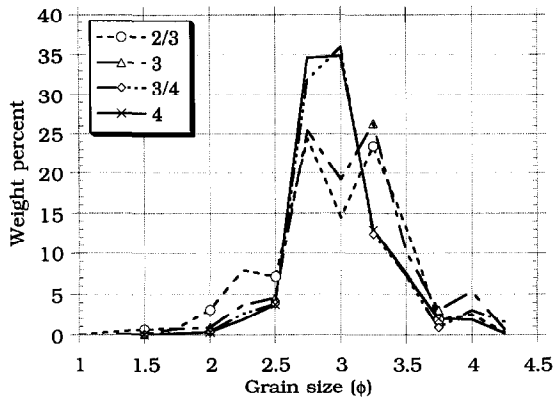

Fig. 4. Grain-size distribution of sand samples retrieved from four traps deployed during July 11–12, 1993.

coarser than the trapped sand samples (erosional mode). The coarse mode comprised a greater percentage of material in the surface sand samples than it did in the trapped sand samples. The coarse mode of surface-sand decreased gradually as a function of increasing elevation of the climbing dune such that, i.e. at sample # 4, it was not present. At the base of the climbing dune (location # 2), wind shear stress diminished and consequently little sand was trapped. Most of the sand on the surface at the base area was between 1.5 to 2.5 ϕ. Unimodal sand only was found in the traps located at the upper part of the dune (traps # 3 and # 4) and the surface sand near trap # 4. Similar results were achieved in other state sequences of samples also taken during the summer period.

The average and standard deviation results of five samples of surface and trapped sand are presented in Table 1. Results show that the surface sand was in the range of 2.2–2.7 ϕ whereas trapped sand was in the range of 2.7–3.0 ϕ. Together they cover the range of 2–3 ϕ, known as the average size of aeolian sand (Ahlbrandt, 1979). The surface sand was decreasing in size with height (except for the sample that was taken in the winter period), whereas the trapped sand was increasing in grain size with gain in elevation along the surface of the dune. A statistical *t*-test done on the mean and standard deviation values of the samples from the surface and trapped sand indicated that, except for three cases (location # 4 on August 11, 1993, and # 3/4 and 4

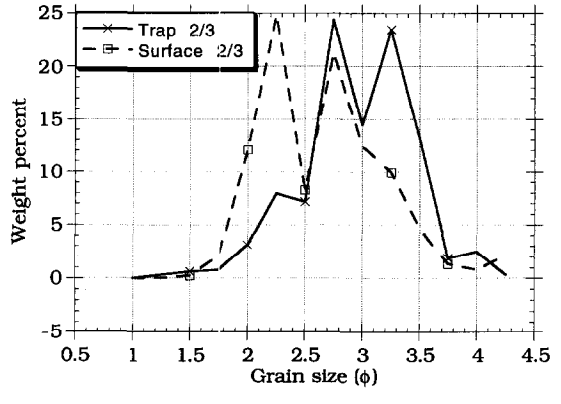

Fig. 3. A comparison between the grain-size distribution retrieved from the surface and trap at point 2/3 in July 1993.

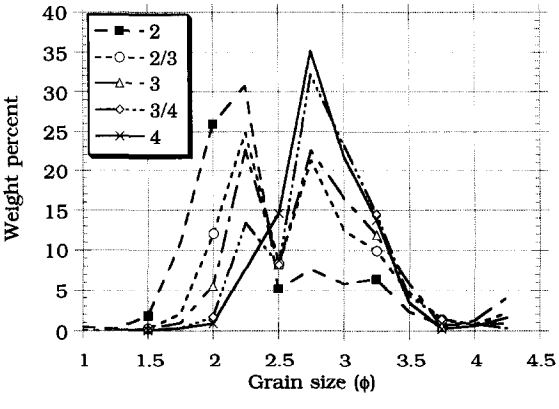

Fig. 5. Grain-size distribution of sand samples retrieved from the surface of the climbing dune near the traps deployed during July 11–12, 1994.

on July 12, 1994), the surface sand was different from the trapped sand at the 0.01 level of significance.

The standard deviation of the samples was mostly in the 'well-sorted' scale with few (> 0.5) in the 'moderately well-sorted' scale (Folk and Ward, 1957; Friedman, 1962). The trapped sand had better sorting than surface sand. A general tendency of improvement in sorting occurred with increases in elevation along the surface of the dune (Table 1).

Four conclusions are drawn from the results:

(1) At the base of the climbing dune, the surface sand was similar in grain-size distribution to the source sand in the Wadi floodplain area. A gradual decrease in surface-grain size occurred as the dune was climbed, which was indicated by the decrease in the coarse mode toward the crest where the grain-size distribution was unimodal.

(2) The grains of the coarse mode were lag deposits that cannot be moved upslope by the wind shear stress. The effect of the slope was actually 'winnowing' away the fine particles at lower elevations of the slope and leaving behind the only coarsest ones.

(3) The shear stress close to the dune crest was intensified to such a degree that coarse sand could be carried easily in saltation.

(4) The gradual decrease of the surface and coarse mode with the elevation of the climbing dunes and the deficiency of the pronounced coarse mode in the trapped sand was only noticeable in summer and not in winter. The winter storm winds are multidirectional whereas the summer storm winds are mostly from a northerly direction.

2.5. Wind-speed profile measurements

Measurements of wind profiles were taken during the summer months along a line parallel to the northerly wind (Fig. 1). Wind-profile measurements at heights of 25, 50, 100 and 150 cm, were taken on four vertical masts with sixteen Proton Anemometers in which the rotational speed of a 3-cup rotor was measured by means of a photo-electric pulse generator and rate meter. Analog D.C. voltage was obtained which provided a linear correlation with wind velocity. Also used were six shielded and ventilated thermostat temperature probes with a resolution of 0.10°C and three potentiometer wind-vanes. Additionally, temperature measurements were obtained to account for the effect of atmospheric stability on the wind velocity profile as described in the next section. All these sensors were connected to a Grant Squirrel data logger.

Measurements of wind profiles were taken on four points along the slope of the climbing dune. Mast # 1 was located 40 m upwind of the 'toe' of the slope (not shown in the map of Fig. 1). This profile represented the undisturbed wind. Mast # 2 was on the base of the dune, mast # 3 in the middle of the slope, and mast # 4 close to the crest (Fig. 1). Wind-profile measurements were taken on August 3, 1993 and July 1, 1994.

2.6. Analysis of field wind data

An improved method was developed to accurately account for the effect of atmospheric stability on the velocity profiles, i.e., to account for the non-neutral diabatic surface layer. The presence of heating or cooling creates stratification in the near surface layer which dramatically alters the structure of the turbulence. This, in turn, distorts the usually linear profile of mean velocity as a function of logarithmic height to one that is non-linear and consequently, difficult to analyze. The new technique developed, which is an iterative process, accounts for the non-linearities introduced by the diabatic process such as those observed in the desert climate. This method was used to determine u_* and z_0 at the mast # 1 location or at the undisturbed site (the other masts were in regions of accelerations or decelerations flow in which the logarithmic velocity profile equation (Eq. (1)) is no longer valid).

Wind data were reduced to extract values of aerodynamic roughness (z_0) and friction velocities (u_*) in the following manner. Wind profiles in a horizontally homogeneous and thermally neutral surface can be described by:

$$u(z) = (u_*/k)\ln(z - d_0)/z_0 \qquad (1)$$

in which k is the von Kármán constant, z_0 is the aerodynamic roughness length, and d_0 is the zero-plane displacement. Because the profile locations lacked significant vegetation and had small- or moderately-sized roughness elements, d_0 was not included in the reduction process.

Most of the wind data were obtained under conditions of strong solar radiation. Consequently, influences of buoyancy on the wind profile must be considered. Non-neutral conditions, in general, are determined by the value of the flux Richardson number, *Ri*, which involves knowing the values of instantaneous local gradients of both temperature and velocity. Because the actual local gradients are not known, the *Ri* cannot be determined. Instead, a bulk Richardson number, *Rb*, is calculated. The *Rb* is an approximation of the flux Richardson number (*Ri*). The bulk Richardson number is the ratio of buoyant turbulence force to energy gained by turbulence acting on the mean velocity gradient. The bulk Richardson number can be measured more easily than the flux Richardson number. A stability correction factor then can be expressed in terms of the buoyancy length scale, z/L, in which L is the Monin–Obukhov length such that wind profiles in non-neutral conditions can be expressed as:

$$u_\alpha(z) = (u_*/k)(\ln z/z_0 - \Psi) \tag{2}$$

where the function Ψ is effectively a 'correction' function to present the data in a neutral buoyancy situation, Ψ is a function of the buoyancy length scale, z/L.

Values of u_* and z_0 are the two parameters of interest. The aerodynamic roughness is primarily a surface property. The friction velocity, a function of surface roughness and mean wind speed, is required in equations of motion for particle trajectory calculations.

Values of z_0 and u_* can be determined from field measurements using the following technique. Measurements of mean velocity and mean temperature profiles at various heights provide the definition of the bulk Richardsons number (*Rb*), which is defined as:

$$Rb = \frac{gz^2}{T}\left(\frac{\frac{\partial T}{\partial z}|z + \frac{g}{C_p}}{u_z^2}\right) \tag{3}$$

in which g is acceleration from gravity, z is height, C_p is specific heat at constant pressure, u_z is mean velocity, and T is mean temperature, both at height z.

Although temperatures were measured at only two or three heights, the linear relation between the natural logarithm of the height, $\ln(z)$, and temperature, $T(z)$, can define the temperature at all heights. Thus,

$$T(z) = A\ln(z) + B \tag{4}$$

where A and B are constants, the slope of this curve is:

$$\frac{\partial T}{\partial Z} = A/z \tag{5}$$

The iterative nature of this technique requires an initial estimate of z_0. Unfortunately, the stability functions Ψ and L are known accurately only for values of the flux Richardson number, not the bulk Richardson number. Thus, it is necessary to estimate the flux Richardson number from the bulk Richardson number. The conversion of bulk Richardson number to the flux Richardson number follows the outlined eight steps given below.

Step 1: calculate Rb using Eq. (3); the ratio $\partial T/\partial z$ is approximated from the logarithmic-linear profile.

Step 2: estimate $z_0 = \exp(u_a)$, where u_a is the z-intercept of the plot of u_a versus logarithm z (z being the anemometer height).

Step 3: calculate *Ri* (initial estimate is $Ri = Rb$); if $Ri < 0$ (air is unstable) then use:

$$x = (1 - 16Ri)^{1/4} \tag{6}$$

$$\Psi = 2\ln\left(\frac{1+x}{2}\right) + \ln\left(\frac{1+x^2}{2}\right) - 2\tan^{-1}x + \frac{\pi}{2} \tag{7}$$

$$\phi = (1 - 16Ri)^{-1/4} \tag{8}$$

$$Ri = Rb\left(\frac{\ln\frac{z}{z_o} - \Psi Ri}{\phi Ri}\right)^2 \tag{9}$$

If $Ri > 0$ (air is stable) then use:

$$\phi - \sqrt{\frac{Rb}{Ri}}\,|\ln\left(\frac{z}{z_0}\right) - \Psi Ri| \tag{10}$$

$$\Psi = \frac{-\beta Ri}{(1 - \beta Ri)} \tag{11}$$

in which $\beta = 7$,

$$Ri = Rb\left(\frac{\ln\frac{z}{z_0} - \Psi Ri}{\phi Ri}\right)^2 \quad (12)$$

These equations are iterated until Ri converges to a constant value.

Step 4: calculate the stability length, L; if $Ri < 0$ (air is unstable) then use:

$$L = \frac{z}{Ri} \quad (13)$$

If $Ri > 0$ (air is stable) then use:

$$L = \frac{z(1 - 5Ri)}{Ri}. \quad (14)$$

Step 5: calculate $\Psi\{z/L\}$ if $L < 0$ then (air is unstable):

$$x = (1 - 16Ri)^{1/4} \quad (15)$$

$$\Psi = 2\ln\left(\frac{1+x}{2}\right) + \ln\left(\frac{1+x^2}{2}\right) - 2\tan^{-1}x + \frac{\pi}{2} \quad (16)$$

If $L > 0$ (air is stable) then use:

$$\Psi = \frac{-7z}{L} \quad (17)$$

Step 6: calculate u_*:

$$u_* = \frac{ku_a}{\ln\frac{z}{z_0} - \Psi} \quad (18)$$

in which k is the von Kármán constant (0.4) and u_a is wind speed at one specific height.

Step 7: plot ($\ln z - \Psi$) versus u_a; least-squares fit where z_0 is the z-intercept value.

Step 8: select a new value of z_0 which is the average between the initially estimated z_0 value (step 2) and the least-squares determined z_0 value (step 7). Repeat steps 1 through 7 with the updated value of z_0 as the new initial estimate in step 2. Repeat this process until z_0 converges to acceptable limits or a specified uncertainty, i.e., (z_0 initial)/(z_0 final) less than a prescribed numerical value, such as 0.0001.

The above algorithm (Eqs. 1–18) has been written in FORTRAN 77 for a computer solution. The program required two input files; an anemometer elevation file and a wind velocity and temperature data file.

The output includes the displacement heights per wind profile and the boundary-layer information. Also it has information on each profile including: the initial z_0 and initial u_* (after the stability correction is applied), Richardson number (Ri), Monin–Obukhov similarity length (L), explained variance (R^2) of velocity as a function of logarithm (z), and an index indicating whether the profile was neutral, converged, diverged, or oscillated. At the end of the file the mean z_0 (geometric mean), the upper and lower standard deviations of z_0, and other statistics are listed.

Several checks were performed to ensure the reliability and consistency of the estimates of wind profile parameters. Plots of z_0 versus the Richardson number show a slight tendency for an overestimation of the temperature gradient because of imperfect shielding of temperature probes. Overall, the typical profiles converged quickly to a constant value of z_0 and constant value of u_*.

3. Wind-tunnel experiments

3.1. Facility

The UC Davis Atmospheric Boundary-Layer Wind Tunnel (ABLWT) was used in the present study. The tunnel, an open-return type, has an overall length of 21.3 m as shown in Fig. 6. The entrance section had a bell-mouth shape to produce a contraction area that minimized the free-stream turbulence level of the air as it passed through the section. A commercially available air-filter followed the contraction area. The filter reduced the large-scale pressure fluctuations of the flow and limited the size of airborne particles entering the wind tunnel. Large-scale turbulence was reduced by honeycomb flow straighteners. Three triangularly shaped spires were placed directly downstream of the flow straighteners to provide favorable turbulent characteristics in the boundary-layer flow.

The section of flow development was 12.2 m long and had walls that diverge to reduce the streamwide

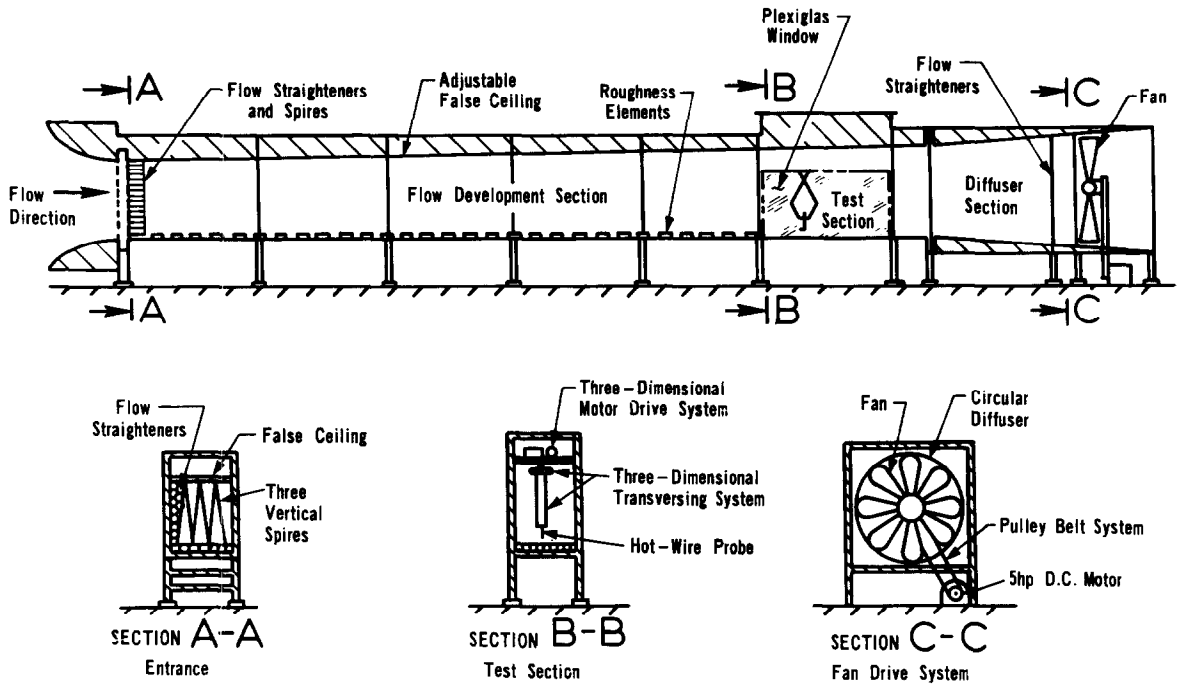

Fig. 6. Diagram of the University of California Atmospheric Boundary Layer Wind Tunnel (ABLWT) showing entrance cone, flow straighteners, spires, adjustable false ceiling, roughness elements, test section, diffuser section, and fan.

pressure gradient. Roughness elements (0.09 m × 0.20 m × 0.06 m) were placed on the floor of this section to artificially thicken the boundary layer. Thick boundary-layer flow was desired because larger models could be tested and measurements of higher resolution could be made. The UC Davis wind tunnel was specifically designed to develop a boundary-layer thickness of about a meter with maximum free-stream wind speed of 4.0 m/s in the test section.

The test section was 2.44 m long, 1.66 m high, and 1.18 m wide in cross-section. The ceilings of the flow development and test sections were adjustable for longitudinal pressure-gradient control. In the test section, a three-dimensional probe positioning mechanism provided fast and accurate (within 1.0 mm) sensor placement. The scissor arms of the mechanism, which provided vertical probe motion, were made of aerodynamically shaped struts to minimize flow disturbances. The diffuser section was 2.37 m long and had an expansion area that provided a continuous transition from the rectangular cross-sectional area of the test section to the circular cross-sectional area of the fan. To eliminate upstream fan swirl effects and avoid flow separation in the diffuser section, fiberboard and honeycomb flow straighteners were placed between the fan and diffuser sections. The fan had eight constant pitch, 1.83 m diameter blades. The variable speed 75 hp D.C.-motor drove the blades with a belt and pulley system.

The flow was conditioned as follows. First, two 1.27 mm mesh stainless-steel screens were placed upstream of the entrance section. Second, a 9.53 mm × 152 mm aluminum Hexcel honeycomb was mounted at the beginning of the long flow development section, followed by four 1.27 mm mesh stainless-steel screens. Third, one foot long 25.4 mm OD PVC-tubing flow straighteners were used to further reduce the large-scale turbulence. Last, three triangularly shaped spires were placed directly downstream of the flow straighteners, and brick-size wooden blocks were placed along the flow development section to artificially thicken the boundary layer.

3.2. Models

A topographic model of the climbing dune, constructed from the topographical contour map that

Fig. 7. Photograph of the 1 : 100 scaled climbing sand dune wind-tunnel model.

was generated in the field from a survey of the dunes with an electronic theodolite, was tested in the wind tunnel. From the cross-section given in the topographical map a wind-tunnel model was constructed at a scale of 1 : 100 (see Fig. 7).

To model wind flow over a climbing sand dune/escarpment in an ABLWT, important similarity criteria have to be met (Cermak, 1974; Isyumov and Tanaka, 1980; Snyder, 1981). White (1996) discusses the similarity criteria for wind-tunnel simulation of dune/saltation flow. For a proper simulation of the full-scale process of wind flow, it is necessary to model the characteristics of naturally occurring wind. Because some parameters, such as gravity, g, or the kinematic viscosity of air, μ, cannot be scaled, therefore similarity criteria are often conflicting in some sense or cannot be simultaneously matched for all full-scale parameters. Therefore, it is necessary to relax certain similarity criteria that are considered less influential than other important parameters (Snyder, 1981).

3.3. Experimental procedures

The wind direction for flow past the scaled model was set by rotating the model. The upstream boundary of the model was carefully contoured to match the height of the roughness elements placed in the flow development section for boundary layer thickening. Small roughness elements (5 mm diameters) were randomly placed on the smooth portion of the surface of the model to maintain the 'rough-wall' boundary-layer flow, for flow directions where the model had long fetches of smooth surface exposed to the wind. A precise ruler was used to measure the scaled height above the test point which included 26 data points measured at discrete heights spaced at approximately equal distances through the height of the boundary layer.

A Dantec Low Velocity Flow Analyzer (Model 54N50) was used for all velocity and turbulence measurements. The Dantec sensor was factory calibrated; additionally, a single hot-wire probe (TSI-1210, T1.5) was used to verify the Dantec calibration. Dantec probe and hot-wire anemometer measurements were found to be in agreement. The present hot-wire anemometry measurements were determined to have an inherent uncertainty of $\pm 5\%$, based upon laboratory calibrations using a TSI Model 1125 calibrator unit.

The probe was vertically mounted on the platform of the three-dimensional traversing mechanism in the test section. The Dantec probe was positioned at a specified location, and flow was digitally sampled

over a 60 s period for velocity and turbulence measurements. The probe was raised to the next height for the next measurements and the procedure was repeated until all profile points for the particular profile were surveyed. Finally, the probe was positioned to a different downstream location over the climbing sand dune model for another profile measurement.

Mean velocity and turbulence data were automatically analyzed on line. The Dantec low velocity analyzer displayed the mean and RMS velocities digitally averaged over a 60 s period. Results were plotted as dimensionless mean velocity and relative turbulence intensity profiles.

The probe was initially placed at an equivalent height of 0.5 m (0.5 mm in the wind tunnel) above the measurement point. For each additional measurement, increments of 0.25 m, 0.50 m, 1.0 m, 5.0 m, and 10.0 m in full scale were used, scaled by a factor of 1 to 100 within the wind tunnel. Up to 26 data points were taken for each velocity profile, unless the wind speed reached the free-stream velocity in which case the measurement was terminated for that particular profile.

4. Numerical solutions of particle motion

A modified version of the United States Federal Aviation Administration (FAA) complex terrain model (Kaimal and Finnigan, 1994) for an escarpment was used to provide an analytical model of the changing surface elevation of the climbing dune as a function of position along its surface. Two supporting ideas justify the use of this model. First, there is a reasonable comparison between the wind-tunnel and field velocity profiles and those predicted from the FAA model. Second, the velocity profiles and shape of the escarpment could be analytically described with equations suitable for computer-generated numerical solutions.

4.1. Velocity profiles

A one-dimensional flow situation and two-dimensional escarpment model was assumed in which velocity in the normal direction to the local surface was zero and velocity, u_a, in the flow (x) direction (i.e., locally parallel to the surface) was a function of normal distance away from the surface only.

In the absence of continuous saltation (i.e., for friction velocities at just above or just below the threshold friction velocity), for fully turbulent boundary layer flow, the logarithmic velocity profile will be given by

$$\frac{u_a}{u_*} = \frac{1}{k}\ln\left(\frac{z}{z_0}\right) \tag{19}$$

where u_* is the friction velocity, z_0 the roughness height and k von Kármán's constant. For a surface of like particles the roughness height may be taken equal to $1/30\ D_p$ and with von Kármán's constant as 0.4, this equation becomes:

$$\frac{u_a}{u_*} = 2.5\ln\left(\frac{z}{D_p}\right) + 8.5 \tag{20}$$

This profile was assumed to be the undistributed one that would ordinarily exist on a flat or horizontal surface.

The geometry of the FAA escarpment model is illustrated in Fig. 8 and is mathematically described by:

$$e = \frac{h}{1 + \left(\frac{x}{L}\right)^2} \qquad \text{for} \quad x < 0 \tag{21}$$

where e is the vertical height of the escarpment above the horizontal plane, i.e., the physical height of the local surface above undisturbed flat ground, h is the vertical height of the escarpment, x is the horizontal distance with a zero value location directly beneath the crest of the escarpment as illus-

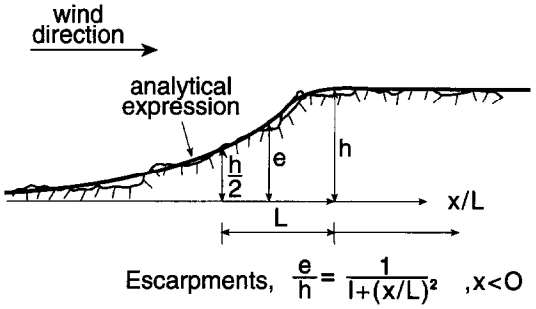

Fig. 8. FAA analytical description of two-dimensional escarpment shape.

trated in Fig. 8, and L is the so-called half horizontal length of the escarpment as measured from the edge of the escarpment to the position where the local surface height decreases to a value of one-half the overall escarpment height, h.

The FAA model uses an approach velocity that is designated by $u_a(z)$, which, in the present case, is given by Eq. (20) above. Here z is always the height above the local ground surface. Local velocities at other locations are designated by $u(x,z)$. The velocity profile will be altered where the escarpment is present. To account for this effect the following procedure was numerically used in the solution of particle trajectories over the escarpment surface. First, a 'velocity perturbation' factor was defined as:

$$\Delta u(x,z) = u(x,z) - u_a(z) \tag{22}$$

and the 'fractional speed-up ratio' was defined as:

$$\Delta S = \frac{\Delta u(x,z)}{u_a(z)} \tag{23}$$

Then the 'amplification factor', A, was given as:

$$A = \frac{u(x,z)}{u_a(z)} = 1 + \Delta S(z) \tag{24}$$

The velocity field was then determined by the exact geometry of the escarpment shape for velocity profiles upwind and over the escarpment up to its crest. Additionally, the maximum wind speed-up factor at the crest was set by the FAA technique which specifies the following guidelines:

$$\Delta S_{max} = 0.8h/L \tag{25}$$

for two-dimensional escarpments. At heights above the crest or escarpment surface for downwind distance of $x > 0$, the exponential decay law given as:

$$\Delta S(o,z) = \Delta S_{max} \exp\left[\frac{-Ez}{L}\right] \tag{26}$$

was used, where $E = 2.5$ for two-dimensional escarpments.

The FAA amplification factors (A) for two-dimensional escarpments were used in the above equations for the present work. To account for the curve escarpment surface (i.e., Eq. (21), with usage of the amplification factors), it was assumed that $A(o,x)$ of the linear escarpment was the same as $A(o,x)$ of parabolic escarpment surface shown in Fig. 8 (Eq. (21)).

The above mathematical descriptions completely specify the complex surface geometry of the escarpment and the analytical flow field above it to account for the resultant increase in wind speed.

4.2. Equations of motion

Forces acting on a saltating particle tending to change its state of motion are a downward force because of its weight and aerodynamic forces produced by the fluid flowing past it. The latter can be resolved into an equivalent lift L, drag D and moment M, as shown in Fig. 9. The direction of the drag is opposite to the direction of V_r, the velocity of the particle relative to the flow. The equations of motion of a particle can be written as:

$$m_p \ddot{x} = L\frac{\dot{z}}{V_r} - D\frac{\dot{x} - u}{V_r} - m_p g \sin\theta \tag{27}$$

$$m_p \ddot{z} = -L\frac{\dot{x} - u}{V_r} - D\frac{\dot{z}}{V_r} - m_p g \cos\theta \tag{28}$$

where m_p is the mass of the particle, and $\dot{x}, \dot{z}, \ddot{x}$ and $\ddot{z}$ are the velocity and acceleration components, respectively.

The magnitude of the relative velocity can be expressed in terms of particle and flow velocities as:

$$V_r = \left[(\dot{x} - u)^2 + \dot{z}^2\right]^{\frac{1}{2}} \tag{29}$$

It generally has been assumed by previous researchers that drag is the primary fluid force acting on a saltating particle away from the surface and that lift is very important at very small heights where the influence of the surface becomes important. The effects of lift and drag are customarily expressed in terms of the lift and drag coefficients C_D and C_L, defined by:

$$L = \frac{1}{2} C_L A_p \rho V_r^2 \tag{30a}$$

$$D = \frac{1}{2} C_D A_p \rho V_r^2 \tag{30b}$$

where A_p is the cross-sectional area of the particle.

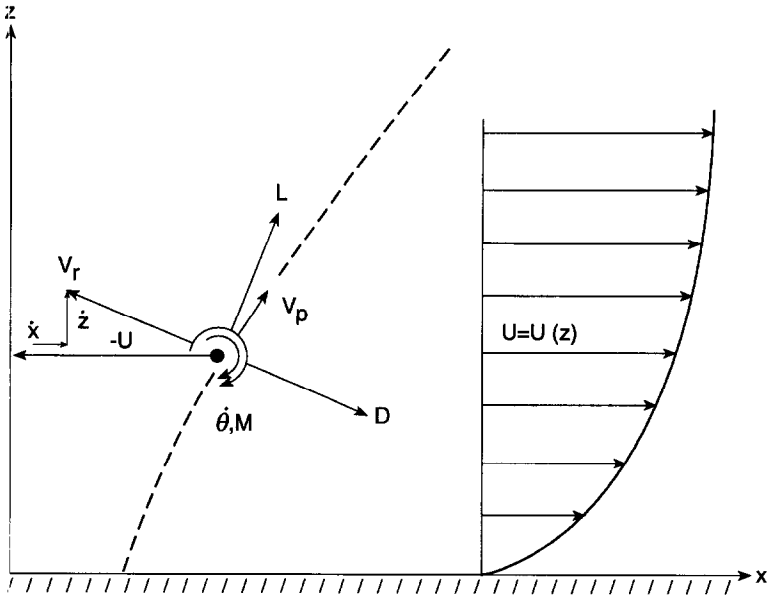

Fig. 9. Local coordinate system z–x showing a particle and its trajectory (dashed line) with velocity profile $U(z)$. L is particle lift, D is particle drag, V_p is particle velocity, M is the moment of the particle, $\dot{\theta}$ is the spin rate of the particle and V_r is the relative velocity of the particle.

If particles are assumed spherical and of uniform density, then equations of motion including lift and drag forces simplify to:

$$\ddot{x} = -\frac{3}{4}\frac{\rho}{\rho_p}\frac{V_r}{D_p}\left[C_D(\dot{x}-u) - C_L\dot{z}\right] - g\sin\theta \tag{31}$$

$$\ddot{z} = -\frac{3}{4}\frac{\rho}{\rho_p}\frac{V_r}{D_p}\left[C_D\dot{z} + C_L(\dot{x}-u)\right] - g\cos\theta \tag{32}$$

4.3. Lift and drag coefficients

Initial conditions are same as those used by White et al. (1976) and White (1979). Initially, the particle is at rest on the surface, and as wind speed is increased above the threshold, particles begin to move. Expressions for the lift coefficients are presented by White et al. (1976). The drag coefficient of a sphere is strongly dependent on the Reynolds number. A number of empirical representations for this dependence have been developed. Perhaps the best of these is given in the paper by Morsi and Alexander (1972), who derived a set of equations expressing relationships between the drag coefficient and Reynolds number over the entire Reynolds number range. These equations were used to calculate drag coefficients needed in the numerical integrations performed in the present work.

5. Discussion of results

5.1. Field measurements

The calculation of shear velocity on slopes from the field wind profiles was problematic. The differential 'speed-up' of the airflow over the slope produced non-logarithmic wind profiles near the surface. Only the velocity profiles measured by mast # 1 (see Fig. 1), the undisturbed upwind profiles, were logarithmic in nature.

The shear velocity for mast # 1 locations was calculated according to the method outlined in the analysis of the wind data presented in Section 2.6 by using Eq. (19). The shear velocity was calculated

according to the logarithmic change in wind speed with height from the relationship:

$$z = z_0 e^{\frac{ku_z}{u_*}} \tag{33}$$

which yielded a value of $z_0 = 8 \times 10^{-4}$ m with a $\sigma = \pm 6.76 \times 10^{-4}$ m.

The wind profiles taken on masts 2, 3 and 4 were nonlogarithmic in nature. The friction speed values for the slope masts were estimated from the following technique. As the wind flow passes over an escarpment, as in the present case, the air speed will increase (or experience a local acceleration) because of the presence of the escarpment. This acceleration of air disrupts the logarithmic profile; however, at the surface the velocity profile becomes approximately linear as a function of height and generally extends some distance outwards away to the surface. Thus, the local shear stress may be estimated as the rate change of velocity with height which would be constant over the near surface linear portion of the profile. In that case, knowing friction speed upwind at the relatively undisturbed location, i.e., mast # 1, it was possible to estimate the rates of local shear on the slope from the following equation:

$$\tau_{(x/L)} \cong \tau_{(\text{undist.})} \left[\frac{U_{25\,\text{cm}(x/L)}}{U_{25\,\text{cm}(\text{undist.})}} \right] \tag{34}$$

Here the local shear stress $\tau_{(x/L)}$ is assumed equal to the undisturbed value multiplied times the ratio of mean wind speed as measured at the lowest height (25 cm), between the local to undisturbed values. Results are presented in Table 2. The shear velocity is related to the shear stress according to the equation:

$$u_* = \sqrt{\frac{\tau}{\rho}} \tag{35}$$

where ρ is the dry air density at 35°C (1.146 kg m^{-3}).

The estimated shear stress and shear velocity were viewed only as approximate; however, they exhibit trends that were consistent with carefully carried out wind-tunnel experiments and field data (Gong and Ibbetson, 1989; Wiggs et al., 1994).

Gong and Ibbetson (1989) performed detailed wind-tunnel measurements of the flowfields around several surface shapes, one of which was similar to the two-dimensional climbing dune or escarpment shape. They measured stress along the surface of the escarpment (their fig. 12d) and found approximately a two-third stress decrease at the base of the slope as compared to the undisturbed value. Midway along the slope surface stress increased to about 58% greater than the undisturbed value and at the top of the escarpment surface stress was approximately 170% that of the undisturbed value. These measurements translate into friction-speed changes of about −18%, +26% and +130% undisturbed friction speed for the base, mid-point and top of escarpment, respectively. These match the wind-tunnel qualitative trends and the field transport data and are reasonably

Table 2
Results of shear stress (in N/m^2) and shear velocity (in m/s) for the four wind profiles ($U_{*t} = 0.17 - 0.18 m/s$)

Mast run	τ_1	u_{*1}	τ_2	u_{*2}	τ_3	u_{*3}	τ_4	u_{*4}
3 Aug. 93								
1	0.029	0.16	0.026	0.15	0.033	0.17	0.053	0.22
2	0.029	0.16	0.021	0.13	0.032	0.17	0.048	0.21
3	0.029	0.16	0.020	0.13	0.032	0.17	0.050	0.21
4	0.016	0.12	0.014	0.11	0.014	0.11	0.032	0.17
6	0.033	0.17	0.022	0.14	0.032	0.17	0.053	0.21
7	0.041	0.19	0.027	0.15	0.037	0.18	0.053	0.22
8	0.029	0.16	0.021	0.13	0.030	0.16	0.045	0.20
9	0.022	0.14	0.016	0.12	0.021	0.13	0.037	0.18
1 July 94								
1	0.046	0.20	0.039	0.18	0.052	0.21	0.086	0.27
2	0.065	0.24	0.042	0.19	0.061	0.23	0.098	0.29
3	0.061	0.23	0.039	0.18	0.055	0.22	0.089	0.28
4	0.037	0.18	0.021	0.14	0.031	0.16	0.055	0.22

well predicted by Eq. (37), with $n = 1$ as shown below.

The results show that the shear stress is decreasing from mast # 1 to mast # 2 on the slope and from there it increases toward the crest. This regression curve of the rate of growth in shear stress fits the following exponential equation where $\tau_{(X/L)}$ was the shear stress at point $(X)/(L)$, $\tau_{(0)}$ was the shear stress at the crest $(X/L = 0)$, and n was the exponent of e.

$$\tau_{(x/L)} = \tau_{(0)} e^{n(x/L)} \tag{36}$$

According to Eq. (35) the shear velocity becomes

$$u_{*(x/L)} = u_{*(0)} e^{n(x/2L)} \tag{37}$$

where $u_{*(x/L)}$ was the shear velocity at point x/L, u_{*_0} was the shear velocity at the crest $(x/L = 0)$, and n was the exponent of e. The value of n for all present cases measured was $n = 1 \pm 10\%$.

The value of $n = 1$ provided a remarkable fit of $\tau_{(x/L)}$ (Eq. (36)), and of $u_{*(x/L)}$ (Eq. (37)), for all locations along the slope independent of date of measurement, and was found to be within an uncertainty of $\pm 10\%$ which is generally considered acceptable for field data correlation.

5.2. Sand flux

The results of sand-flux measurements taken during five different periods are shown in Fig. 10. Sand-trap data suggest that an exponential increase in sand flux occurs with the height of the dune. The increase in sand flux was related to the increase in wind shear stress along the sloping portion of the dune. Additionally, the funneling shape of the complex three-dimensional dune geometry causes sand to be transported along the westerly slope toward the upper trap. The dune resembled the apex of a funnel that collected material coming from all directions (i.e., not only the lower portions, but also the east and west lateral sides as well).

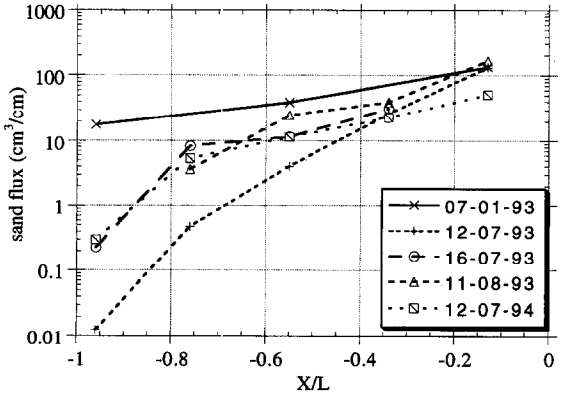

Fig. 10. Sand flux along the slope of the climbing dune during various periods of measurements.

This alters the two-dimensional aspect of the problem; nonetheless, the surface stress should be directly related to sand transport at that location. Thus, the slope effect and three-dimensional flow effects are merged together producing a single value of stress that controls the sand transport at each location on the surface of the climbing dune. The profiles of wind-tunnel velocity are useful in determining local flow acceleration; however, they cannot be used exclusively to estimate friction speeds since the flow is not in equilibrium and the effects of local pressure gradients are important yet unknown. Thus, velocity profiles display qualitative features of surface-stress distribution but not quantitative values of friction speeds. The traps were left in the field for several days and are not directly related to the shear stress measurements presented in Table 2.

Four measurements were taken in the summer under a northerly wind regime. One was taken in winter (January), when wind came from several directions. The summer data show that the trap at the plinth of the dune $(x/L = -0.96)$ captured a very small amount of sand, whereas the other traps (from $x/L = -0.76$ to -0.13) had a gradual increase in sand flux. The exponential equations of the sand flux increase with the upslope were different for the various periods of measurements. The rate of sand transport, generalized as q, is proportional to the friction speed cubed.

According to Eqs. (36) and (37), the sand flux for the climbing dune in the field will be:

$$q_{(x/L)} = q_{(0)} \exp\left[\frac{3n}{2}(x/L)\right] \tag{38}$$

where $q_{(x/L)}$ was the amount of sand trapped at point x/L, and $q_{(0)}$ is the amount trapped at the crest $(x/L = 0)$.

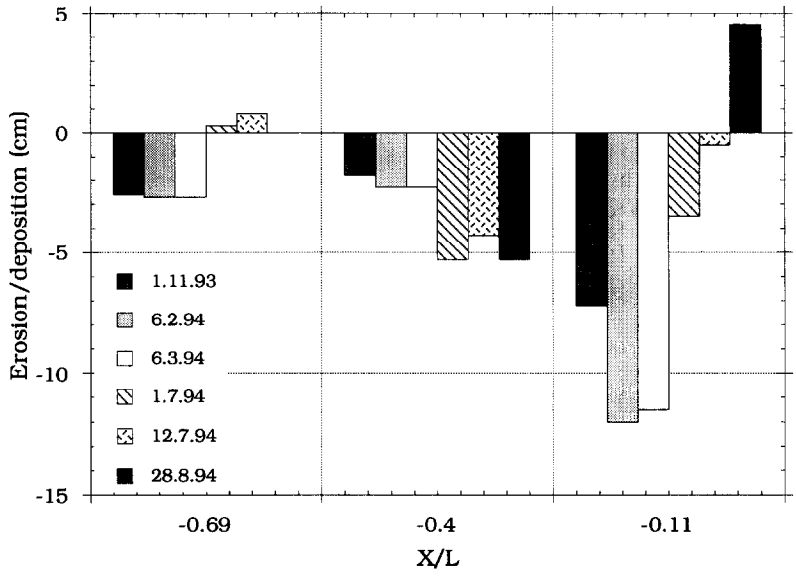

Fig. 11. Erosion pin data as measured along reference points 2, 5, and 8 (Fig. 1).

The average value of n obtained from the sand flux measurements was 1.13 or about 13% larger than predicted with the previous value of $n = 1$ form Eq. (37). Thus, it was assumed that the traps used in the field were not efficient enough in trapping sand, because the higher the value of n, the lower the amount of sand trapped in the slope.

5.3. Erosion pins

The locations of the erosion pins are shown on the map of Fig. 1. Results along two lines, one along points 2, 5 and 8 (Fig. 11) and the other along points 6–9 (Fig. 12), show clearly that erosion of the surface occurred in winter and during the next sum-

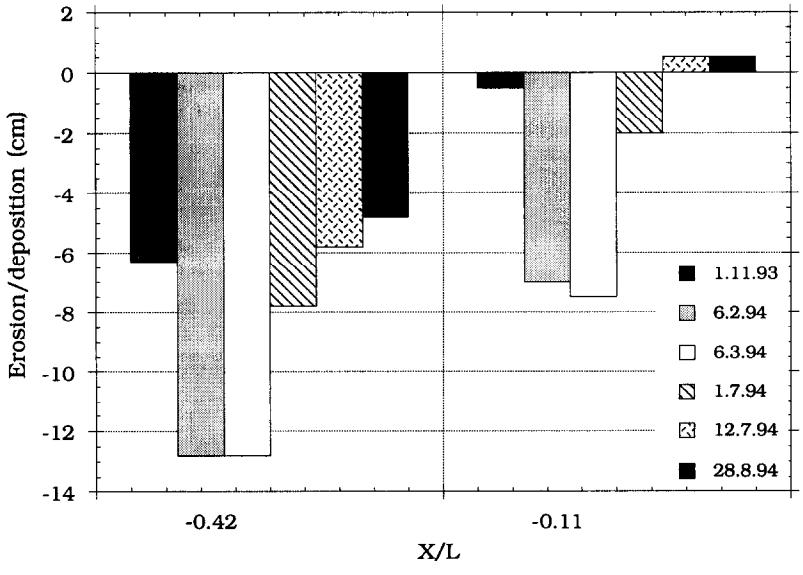

Fig. 12. Erosion pin data as measured along reference points 6–9 (Fig. 1).

mer the surface returned to its previous condition by accretion. The most dramatic changes occurred at the mid-slope and close to the crest.

6. Wind-tunnel measurements

Profiles of mean velocity and turbulence intensity along the surface of the climbing dune were acquired in the ABLWT at UC Davis. A reasonable correlation exists between the scaled up wind-tunnel and field results and those predicted from the FAA model (Fig. 13). The field data had a better correlation to the FAA results than the wind-tunnel data. The wind-tunnel results predict greater mean wind speeds above 2 m height. The critical region in this comparison of wind-tunnel profiles to FAA profiles, however, is ground level. This is the region where particle motion occurs and where it is important to have a good empirical model, such as the FAA model, to use in the solution of particle trajectories. As was observed from the data, most of the profiles in the lower two meters have good comparisons between the wind-tunnel measurements and the FAA empirical predictions. Fig. 13 displays a comparison of the field data taken on August 3, 1993 (run # 9) with the wind-tunnel and FAA data. The locations 1–4 refer to the measurement locations for both field and

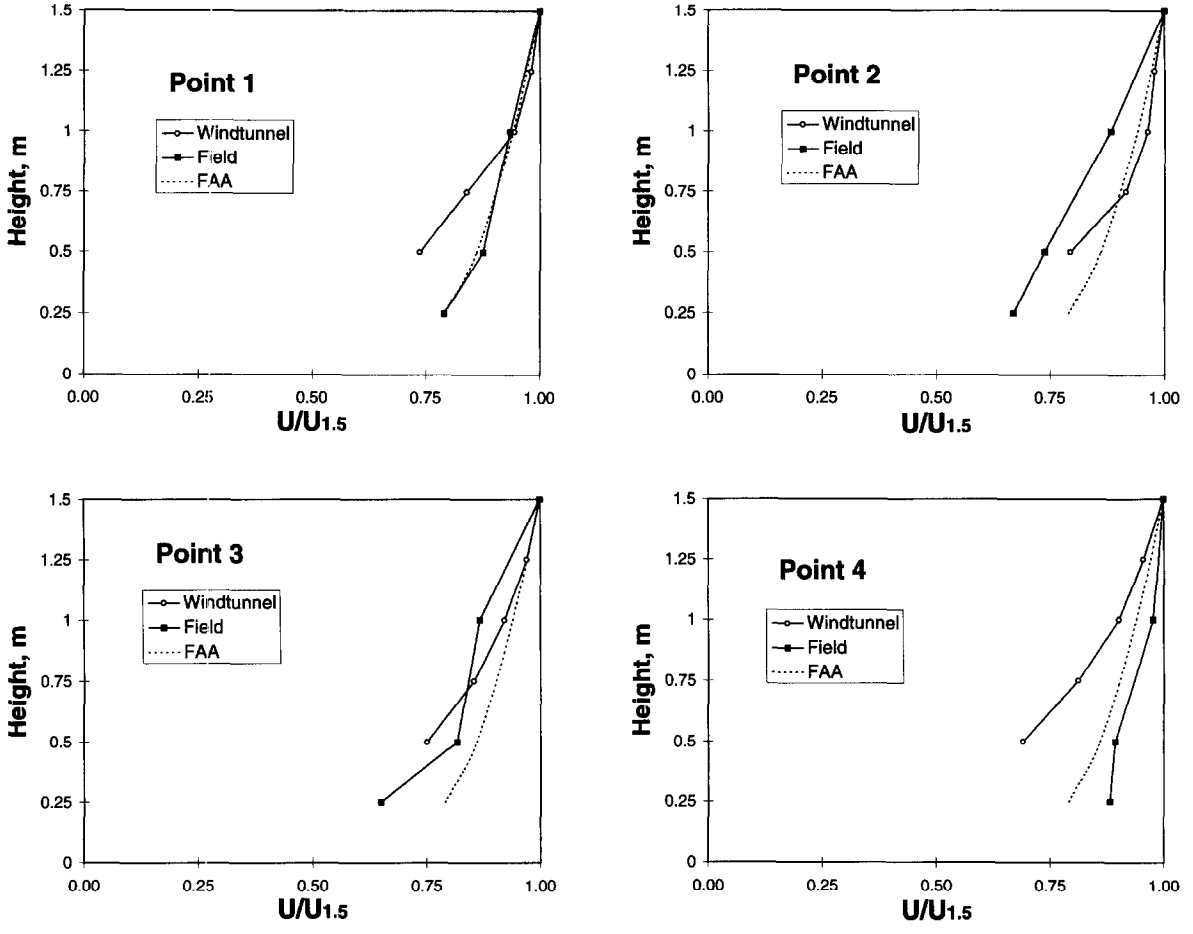

Fig. 13. The mean normalized wind speed is given as a function of full-scale height for wind-tunnel field and FAA data. Four locations (1, 2, 3 and 4) are presented and correspond to the positions identified in Fig. 1. The wind-tunnel heights are increased by the model scale factor which was 100, i.e., 1 cm equal to 1 m.

wind-tunnel and are given in Fig. 1. The FAA profile was calculated from the technique outlined in Section 4. Point # 1 is upwind of the climbing dune and its location is not shown on Fig. 1 because it is off the figure area. It represents approximately the undisturbed approaching wind profile. Point # 2 is at the base of the dune; points # 3 and # 4 are midway along the slope from the base to crest and at the crest, respectively. The measurement height in the wind tunnel was multiplied by scale factor (100) to allow for full-scale comparisons. The measured wind speed was self normalized by the wind speed measured at a height of 1.5 m. As may be observed from Fig. 13 the three curves (wind-tunnel, field and FAA data) all are reasonably close to each other and no preferred trend is apparent. Consequently, the FAA model was used in the numerical solutions because of this feature and it can be empirically calculated for any position on the escarpment.

6.1. Numerical solution of particle trajectories

A typical path of the trajectory of the particle is shown in Fig. 14. The height of the escarpment at its crest was set at 20 m and the length $L/2$ was determined, from Fig. 1, to be 27.5 m (assuming an average escarpment angle of about 20 degrees as measured both in the field and from the map). The undisturbed value of shear speed was set at five velocities of 10, 20, 30, 40 and 50 cm/s. The trajectories of six particles (130, 170, 242, 320, 544, and 1000 μm in size) as well as the jump height, and the impact speed and angle, were calculated for seven positions along the escarpment surface: (1) the upwind undisturbed profile at 1 km upwind (same as flat or horizontal trajectory calculations); (2) $x/L = -1.38$; (3) $x/L = -1.00$, the base of the escarpment; (4) $x/L = -0.58$; (5) $x/L = -0.15$; (6) $x/L = 0.0$ (at the escarpment crest); and (7) $x/L = +0.38$. The same calculations were made to five slopes whose inclinations were 5, 10, 15, 20, and 25 degrees. The four parameters of the saltating grain mentioned above are shown in Fig. 15. $H_{max} = \max(h_a - h_b)$ where h_a are the points on the trajectory path and h_b are the reciprocity hill (escarpment) points. To find the length L_S the impact point D had to be determined (see Fig. 15) and then:

$$L_S = |(x_D x_c)/\cos\Theta| \tag{39}$$

The final velocity is the velocity at the impact point D then this was calculated by:

$$V_{\text{final}} = \left(\dot{x}_D^2 + \dot{z}_D^2\right)^{\frac{1}{2}} \tag{40}$$

Two points of integration of the trajectory (the impact point F and a point E nearby) were taken for calculating the impact angle (Fig. 16). The angle Φ was calculated by:

$$\Phi = \arctan\left(\frac{z_E - z_F}{x_E - x_F}\right) \tag{41}$$

then the impact angle was $\Phi + \alpha$.

Results from the trajectory calculations from a slope of 20 degrees (Fig. 17) show which particles stop at the base of the climbing dune and which ones would be able to move to the upper elevations of the surface for the five different shear velocities calculated. The results, for these commonly occurring shear velocities, suggest that particles would soon be depleted from the upper half of the dune because no new particles of the same size would be moving upwards. This feature was observed in the size-distri-

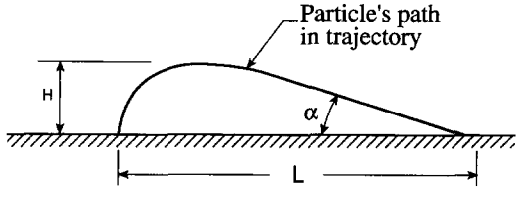

Fig. 14. A typical path of the trajectory of the particle. H is the maximum height the particle obtains in the trajectory, while L is the maximum jump length obtained; α is the collision angle which the path of the particle makes with the surface upon impact.

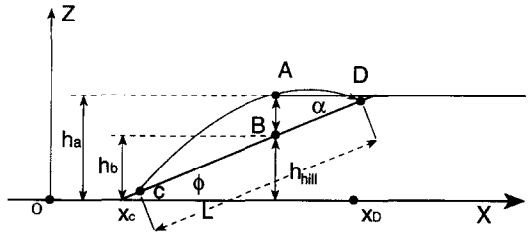

Fig. 15. The path of the trajectory of the particle on the slope in which the trajectory length, jump height, impact speed and angle of the saltating grain were calculated.

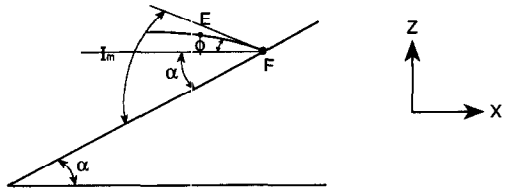

Fig. 16. The impact angle ($\phi \pm \alpha$) of the saltating sand on the slope.

bution analysis taken in the field samples (Fig. 5). Particle trajectories at the crest of the dune and further downwind display extra-long path lengths ranging from 2 to 3 times the respective undisturbed path lengths. Again this feature was consistent with field observation, with the exception of the formulation of a second dune on top the escarpment surface. This dune was caused by a flow separation and a resulting recirculation region occurring just downwind of the crest area on the escarpment. This feature of the field flow was not modeled.

General results were that all particle motions (path lengths) were diminished toward the lower half of the slope (between $x/L = -1.0$ and -0.58) of the climbing dune. The motion of larger-sized particles

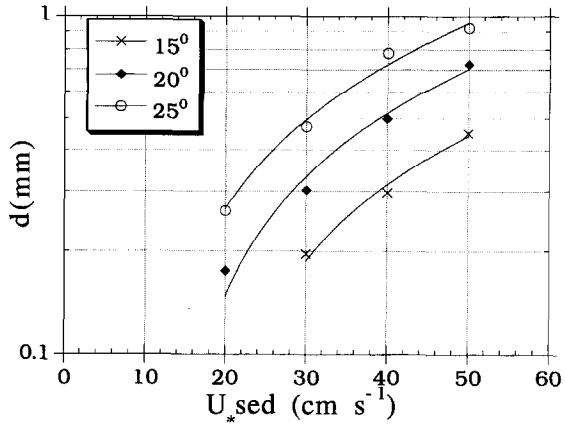

Fig. 18. U_* sed vs. grain size (d) for three slopes of 15, 20, and 25 degrees, at the base of the escarpment ($x/L = -1.0$).

was more adversely affected than the motion of smaller, 130 μm sized, particles. The results of the model calculations agree with field observation with the single exception of increase in sand flux along the slope.

The shear velocity at which the saltating grains have a very small trajectory length (< 7 cm) is considered as the sedimentation speed (U^*sed) at

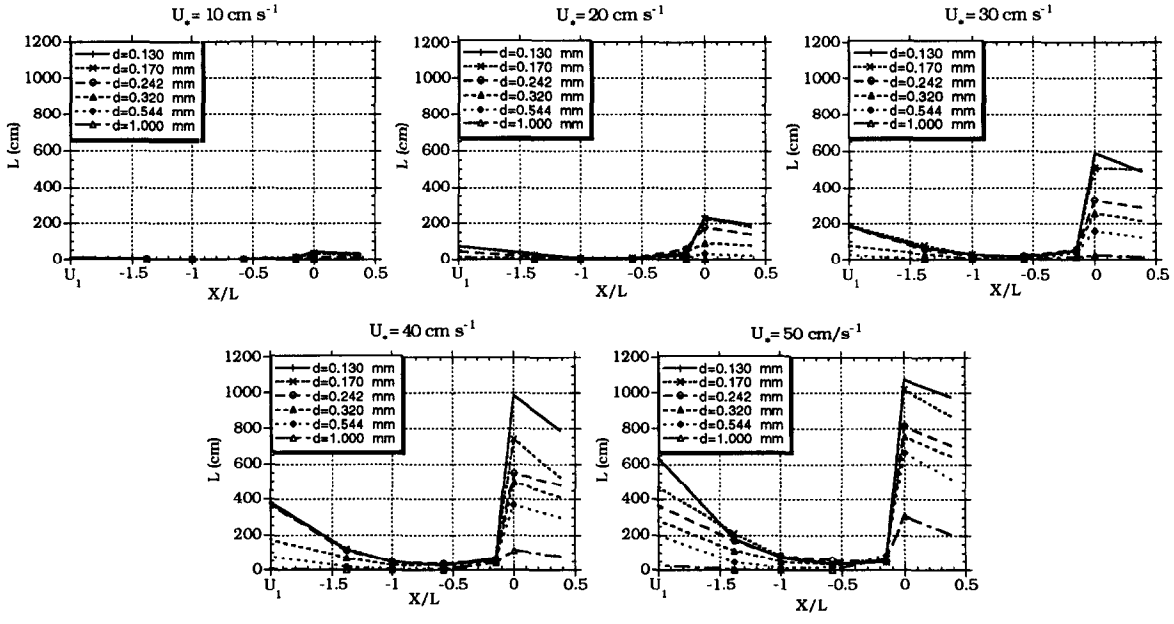

Fig. 17. Trajectory pathlength (L) of saltating grain along a 20 degrees slope of a climbing dune under shear wind velocity of 10, 20, 30, 40 and 50 cm/s. U_1 indicates the undisturbed trajectory pathlength for each shear velocity.

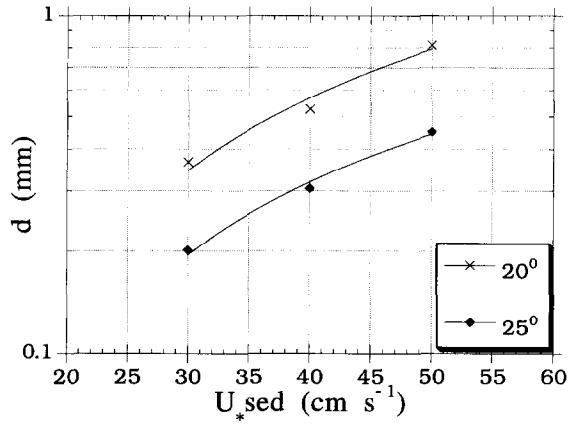

Fig. 19. U_* sed vs. grain size (d) for two slopes of 20 and 25 degrees, at $H/L = -0.58$.

which the grains tend to deposit. This speed is similar to the impact threshold in Bagnold (1941) which is lower than the fluid threshold speed that was measured in the wind-tunnel experiments done recently by Iversen and Rasmussen (1994). The sedimentation speed was calculated twice, once at the base of the escarpment ($x/L = -1.0$) for three slopes of 15, 20, and 25 degrees (Fig. 18) and once at $x/L = -0.58$ for 20 and 25 degrees (Fig. 19). The results at the 20 and 25 degrees slope at the base of the dune (Fig. 18) and of the 20 and 25 degrees slope at $x/L = -0.58$ (Fig. 19) are lower than the data of Iversen and Rasmussen (1994). The 15 degree curve (Fig. 18) and the 25 degree one of Fig. 19, were similar.

7. Synopsis

A three-year collaborative study on the nature and governing natural processes controlling a series of 'climbing sand dunes' that exist in the Negev Desert region of Israel has been conducted. Overall, three main areas of research have been investigated: (1) field measurements of velocity data, particle size distributions, and transport rates of saltation from the climbing dune of Nahal Kasuy; (2) wind-tunnel simulations (at UC Davis) of a model of the climbing dune from the Nahal Kasuy area; and (3) numerical solutions of particle motion as they apply to the conditions occurring on a slope.

Results show an exponential increase in the sand flux with the height of the dune. The increase in sand flux is related to the augmentation in wind shear stress. Because of the funneling shape of the slopes, sand also was carried along the westerly slope toward the upper trap, which resembled the apex of a funnel that conveys liquid coming from all sides. Previously, no known measurements were reported in scientific literature of the grain-size distribution along a climbing dune. Therefore, sand was sampled on the climbing dune in two ways: first, samples were taken from the sand traps mentioned above; second, samples were collected directly from the surface of the dune in the same area as the traps. The first samples indicated sand in a state of erosion, whereas the second samples indicated sand in the deposition mode.

Three important conclusions were drawn from the results:

(1) On the toe of the climbing dune, the surface sand was similar in grain-size distribution to the source sand in the Wadi floodplain area. A gradual decrease in surface grain size occurred as the dune was climbed, which was indicated by the decrease in the coarse mode toward the crest where the grain-size distribution was unimodal.

(2) The grains of the coarse mode were lag deposits that could not be moved upslope by the observed wind shear-stress. The effect of the slope was winnowing away the fine particles at lower elevations of the slope and leaving behind the coarser ones.

(3) The gradual decrease of the surface sand coarse mode with the elevation of the climbing dunes and the deficiency of the pronounced coarse mode in the trapped sand was only noticeable in summer when the storm winds were steady from a northerly direction, and not in winter, when the winds were multidirectional.

The ABLWT located at the University of California, Davis, was used in the present study. A topographic model of the climbing sand dune tested in the ABLWT, was constructed from a topographical contour map that was generated in the field from a survey of the dune with an electronic theodolite. An accurate wind-tunnel simulation of the wind flow over the climbing dunes may only be achieved if critical similarity requirements are met. A careful

similitude analysis was carried out to identify and meet these parameters. Extensive wind-profile measurements have been made for the model and compared to field velocity profiles and the FAA model.

A reasonable correlation exists between the 'scaled-up' wind-tunnel results and those predicted from the FAA near-surface wind flow model. Most of the profiles in the lower two meters had reasonable comparisons between wind-tunnel measurements, field measurements, and FAA empirical predictions. Consequently, the FAA model was used in the numerical solutions because of this feature and it can be empirically calculated for any position on the escarpment/dune surface.

Key results from the trajectory calculations are that the 330 μm particles were stopped at the base of the climbing dune and those sized particles already present would be only moved in the upper elevations of the surface. The result, for a commonly occurring friction speed of 30 cm/s, would suggest that the supply of 330 μm particles would be soon depleted from the upper surface of the dune because no new particles of the same size would be moving upwards. This feature was observed in the size-distribution analysis taken in the field samples. Also, movement of 230 μm particles would be stopped in the lower one-third height region of the dune. This is because the diminished surface stress in this region was insufficient to move the 230 μm particles. This feature also was consistent with the results of the field samples taken in this location on the dune (Fig. 5). Lastly, the 130 μm particles, although slowed down, did continue saltating to the crest of the dune which also was observed in the field data (Fig. 5).

Lastly, numerical solutions of particle motion along plane inclined slopes were performed over a range of slope angles (15 to 25 degrees), over a range of friction speeds (10 to 50 cm/s), and over a range of particle size (130 to 1000 μm in diameter). The major findings show that the pathlengths of all particles were suppressed at the base area of the escarpment by the decreased values in friction speed. This was observed in both field and wind-tunnel measurements. The 1 mm sized particles were more adversely affected than the 100–200 μm particles. It is worth noting that all particle trajectories exhibited a consistent decrease in particle pathlengths in the lower half of the slope.

Acknowledgements

This research was supported by Grant No 90-00253 from the United States–Israel Binational Science Foundation (BSF), Jerusalem, Israel.

References

Ahlbrandt, T.S., 1979. Textural parameters of eolian deposits. In: McKee, E.D. (Ed.), A Study of Global Sand Seas. U.S. Geol. Surv., Prof. Pap. 1052, 21–51.

Bagnold, R.A., 1941. The Physics of Blown Sand and Desert Dunes. Methuen, London.

Burkinshaw, J.R., Illenberger, W.K., Rust, I.C., 1993. Wind-speed profiles over a reversing transverse dune. In: Pye, K. (Ed.), The Dynamics and Environmental Context of Aeolian Sedimentary Systems. Geological Society, Bath, pp. 25–36.

Cermak, J.E., 1974. Applications of fluid mechanics to wind engineering—a Freeman scholar lecture. Presented at the Winter Annual Meeting of the American Society of Mechanical Engineers, New York. J. Fluid Eng. 97, 9–38.

Folk, R.L., Ward, W.C., 1957. Brazos River bar: a study in the significance of grain size parameters. J. Sediment. Petrol. 27, 3–26.

Friedman, G.M., 1962. On sorting coefficients, and the log-normality of the grain-size distribution of sand stones. J. Geol. 70, 737–756.

Gong, W., Ibbetson, A., 1989. A wind tunnel study of turbulent flow over model hills. Boundary-Layer Meteorol. 49, 113–148.

Hardisty, J., Whitehouse, K.J.S., 1988. Evidence for a new sand transport process from experiments on Saharan dunes. Nature 332, 532–534.

Hunt, J.C.R., Leibovich, S., Richards, K.J., 1988a. Turbulent shear flow over low hills. Q.J.R. Meteorol. Soc. 114, 1435–1470.

Hunt, J.C.R., Richards, K.J., Brighton, P.W.M., 1988b. Stratified shear flow over low hills. Q.J.R. Meteorol. Soc 114, 859–886.

Isyumov, N., Tanaka, H., 1980. Wind tunnel modelling of stak gas dispersion — difficulties and approximations. In: Cermak, J.E. (Ed.), Wind Engineering. Pergamon Press, Oxford, pp. 987–1001.

Iversen, J.D., Rasmussen, K.R., 1994. The effect of surface slope on saltation threshold. Sedimentology 41, 721–728.

Jackson, P.S., Hunt, J.C.R., 1975. Wind flow over a low hill. Q.J.R. Meteorol. Soc. 101, 929–955.

Jensen, N.O., Zeman, O., 1985. Perturbation in mean wind and turbulence in flow over topographic forms. In: Barndorff-Nielsen, O.R., Møller, J.T., Rasmussen, K.R., Willetts, B.B. (Eds.), Proceedings of the Int. Workshop of the Physics of Blown Sand. Dept. Theoretical Statistics, Inst. of Mathematics, Univ. Aarhus, Mem. No. 8, pp. 351–368.

Kaimal, J.C., Finnigan, J.J., 1994. Atmospheric Boundary Layer Flow. Oxford University Press, New York.

Lancaster, N., 1985. Variations in wind velocity and sand trans-

port on the windward flanks of desert sand dunes. Sedimentology 32, 581–593.

Leatherman, S.P., 1978. A new aeolian sand trap design. Sedimentology 25, 303–306.

Lettau, K., Lettau, H., 1978. Experimental and micrometeorological field studies of dune migration. In: Lettau, H.H., Lettau, K. (Eds.), Exploring the World's Driest Climate. Centre for Climatic Research, Madison, pp. 110–147.

Morsi, S.A., Alexander, A.J., 1972. An investigation of particle trajectories in two-phase flow systems. J. Fluid Mech. 55, 193–208.

Mulligan, K.R., 1988. Velocity profiles measured on the windward slope of a transverse dune. Earth Surf. Processes Landforms 13, 573–582.

Pye, K., Tsoar, H., 1990. Aeolian Sand and Sand Dunes. Unwin Hyman, London.

Rosen, P.S., 1979. An efficient, low cost, aeolian sampling system. Scient. Tech. Notes, Current Res. Part A, Geol. Surv. Can. Pap. 78-1A, pp. 531–532.

Snyder, W.H., 1981. Guideline for Fluid Modeling of Atmospheric Diffusion. U.S. Environmental Protection Agency, Research Triangle Park, NC, EPA/600/8-81-009.

Taylor, P.A., Gent, P.R., 1974. A model of atmospheric boundary layer flow above an isolated two-dimensional hill; an example of flow above gentle topography. Boundary-Layer Meteorol. 7, 349–362.

Tsoar, H., 1976. Characterization of sand dune environments by their grain-size, mineralogy and surface texture. In: Amiran, D.H.K., Ben-Arieh, Y. (Eds.), Geography in Israel. Israel National Committee, International Geographical Union, Jerusalem, pp. 327–343.

Tsoar, H., 1985. Profile analysis of sand dunes and their steady state significance. Geogr. Ann. 67, 47–59.

Tsoar, H., 1986. Two-dimensional analysis of dune profile and the effect of grain size on sand dune morphology. In: El-Baz, F., Hassan, M.H.A. (Eds.), Physics of Desertification. Martinus Nijhoff, Dordrecht, pp. 94–108.

Tsoar, H., Pye, K., 1987. Dust transport and the question of desert loess formation. Sedimentology 34, 139–153.

Walmsley, J.L., Howard, A.D., 1985. Application of a boundary-layer model to flow over an eolian dune. J. Geophys. Res. 90, 10631–10640.

White, B.R., 1979. Soil transport by winds on Mars. J. Geophys. Res. 84, 4643–4651.

White, B.R., 1982. Two-phase measurements of saltating turbulent boundary-layer flow. Int. J. Multiphase Flow 8, 459–473.

White, B.R., 1996. Laboratory simulation of aeolian sand transport and physical modeling of flow around dunes. Ann. Arid Zone 35 (3), 187–213.

White, B.R., Schulz, J.C., 1977. Magnus effect in saltation. J. Fluid Mech. 81, 497–512.

White, B.R., Greeley, R.G., Iversen, J.D., Pollack, J.B., 1976. Estimated grain saltation in a Martian atmosphere. J. Geophys. Res. 81, 5643–5650.

Wiggs, G.F.S., 1993. Desert dune dynamics and the evaluation of shear velocity: an integrated approach. In: Pye, K. (Ed.), The Dynamics and Environmental Context of Aeolian Sedimentary Systems. The Geological Society, Bath, pp. 37–46.

Wiggs, G.F.S., Livingstone, I., Thomas, D.S.G., Bullard, J.E., 1994. Effect of vegetation removal on airflow patterns and dune dynamics in the southern Kalahari desert. Land Degrad. Rehabil. 5, 13–24.

Wipperman, F.K., Gross, G., 1986. The wind-induced shaping and migration of an isolated dune: a numerical experiment. Boundary-Layer Meteorol. 36, 319–334.